nature catalysis

Article

https://doi.org/10.1038/s41929-024-01175-8

Atomic-scale identification of active sites of oxygen reduction nanocatalysts

Received: 5 December 2023

Accepted: 9 May 2024

Published online: 8 July 2024

Check for updates

Yao Yang[1,8,9], Jihan Zhou[1,9], Zipeng Zhao[2,9], Geng Sun[3,9], Saman Moniri[1], Colin Ophus[4], Yongsoo Yang[1], Ziyang Wei[5], Yakun Yuan[1], Cheng Zhu[6], Yang Liu[2], Qiang Sun[7], Qingying Jia[7], Hendrik Heinz[6], Jim Ciston[4], Peter Ercius[4], Philippe Sautet[3,5] ✉, Yu Huang[2] ✉ & Jianwei Miao[1] ✉

Heterogeneous nanocatalysts play a crucial role in both the chemical and energy industries. Despite substantial advancements in theoretical, computational and experimental studies, identifying their active sites remains a major challenge. Here we utilize atomic electron tomography to determine the three-dimensional atomic structure of PtNi and Mo-doped PtNi nanocatalysts for the electrochemical oxygen reduction reaction. We then employ the experimental atomic structures as input to first-principles-trained machine learning to identify the active sites of the nanocatalysts. Through the analysis of the structure–activity relationships, we formulate an equation termed the local environment descriptor, which balances the strain and ligand effects to provide physical and chemical insights into active sites in the oxygen reduction reaction. The ability to determine the three-dimensional atomic structure and chemical composition of realistic nanoparticles, combined with machine learning, could transform our fundamental understanding of the active sites of catalysts and guide the rational design of optimal nanocatalysts.

Nanocatalysts have found broad applications, ranging from fuel cells to catalytic converters and hydrogenation reactions[1–3]. Understanding the active sites and local environment of nanocatalysts has attracted considerable attention from theoretical, computational and experimental studies[4–20]. However, characterizing the three-dimensional (3D) atomic and chemical arrangement of different constituents, as well as structural reconstructions driven by catalytic reactions[21–24], remains elusive. Although a number of experimental methods have been used to study nanocatalysts, each has its limitations. X-ray absorption spectroscopy (XAS) is an important in situ/operando technique for probing the structure and composition of nanocatalysts, but it globally averages a large number of samples and isotopically characterizes nanocatalysts from the surface to the core[25,26]. In situ and environmental transmission electron microscopy (TEM) can image the local heterogeneous structure of nanocatalysts in gas- and liquid-phase reactions, but the resolution and contrast of the images are often hindered[27,28]. To achieve the highest possible spatial resolution, scanning TEM (STEM) and TEM are the methods of choice and have been widely used to characterize the structure and composition of nanocatalysts in a vacuum[8,10,12,16,29–31]. However, both in situ and environmental TEM, as well as high-resolution

[1]Department of Physics & Astronomy and California NanoSystems Institute, University of California, Los Angeles, Los Angeles, CA, USA. [2]Department of Materials Science and Engineering, University of California, Los Angeles, Los Angeles, CA, USA. [3]Department of Chemical and Biomolecular Engineering, University of California, Los Angeles, Los Angeles, CA, USA. [4]National Center for Electron Microscopy, Molecular Foundry, Lawrence Berkeley National Laboratory, Berkeley, CA, USA. [5]Department of Chemistry and Biochemistry, University of California, Los Angeles, Los Angeles, CA, USA. [6]Department of Chemical and Biological Engineering, University of Colorado at Boulder, Boulder, CO, USA. [7]Department of Chemistry and Chemical Biology, Northeastern University, Boston, MA, USA. [8]Present address: School of Engineering, Westlake University, Hangzhou, China. [9]These authors contributed equally: Yao Yang, Jihan Zhou, Zipeng Zhao, Geng Sun. ✉e-mail: sautet@ucla.edu; yhuang@seas.ucla.edu; miao@physics.ucla.edu

S/TEM, provide only two-dimensional projection images of 3D nanocatalysts. Currently, atomic electron tomography (AET) is the only experimental method that is capable of resolving all of the 3D atomic positions of individual nanoparticles[32–36].

Here we use AET to determine the 3D atomic structures of platinum (Pt) alloy nanocatalysts for the oxygen reduction reaction (ORR) in proton exchange membrane fuel cells[37,38]. We investigate the nanocatalysts before and after catalytic activation, observing their 3D structural and compositional changes at the atomic scale (see Methods). The experimental 3D atomic structures obtained after catalytic activation are used for density functional theory (DFT)-trained machine learning (ML) to identify the active sites of the nanocatalysts.

Results

Atomic electron tomography of Pt alloy nanocatalysts

Platinum–nickel alloy (PtNi) and molybdenum-doped PtNi (Mo-PtNi) nanocatalysts with varying nickel (Ni) concentrations were synthesized on carbon black/nanotubes (C/CNT) using an efficient one-pot approach[39,40] (Methods). The nanocatalysts on carbon black were activated after 30 cycles of cyclic voltammetry. The ORR specific activities of PtNi and Mo-PtNi were measured to be 4.8 and 9.3 mA cm^{-2}, respectively, at 0.9 V_{RHE} (Supplementary Fig. 1 and Supplementary Table 1). The increase in ORR activity with the Mo dopant is consistent with previous reports[39–41]. AET experiments on 11 PtNi and Mo-PtNi nanocatalyst particles embedded in carbon nanotubes were performed using annular dark-field STEM (ADF-STEM) (Supplementary Figs. 2–6 and Supplementary Table 2). To minimize the electron dose, a low-exposure data acquisition scheme[33] was used to obtain the datasets, and the structure of the nanocatalysts remained consistent throughout the experiments (Supplementary Fig. 7). After preprocessing, 3D reconstruction, atom tracing and refinement[32,35] (Methods and Supplementary Fig. 8), the 3D atomic coordinates and chemical composition of the nanocatalysts were determined (Fig. 1). The voxel size was calibrated using extended X-ray absorption fine structure (EXAFS) measurements (Methods). The total number of Pt and Ni atoms in each of the 11 nanocatalysts ranges from 4,281 to 14,172 (Supplementary Table 2). According to a previous study[40], a very small fraction (~0.4%) of the Mo dopant is primarily distributed near the vertex and edge sites of the Mo-PtNi octahedron, affecting the overall shape and alleviating the leaching of Ni atoms under the detrimental corrosive ORR conditions. Owing to the very small fraction of the Mo dopant, AET is currently not sensitive enough to distinguish them from the Ni atoms.

Figure 1, Supplementary Fig. 9 and Supplementary Video 1 show the 3D surface morphology, atomic structure and chemical composition of the 11 PtNi and Mo-PtNi nanocatalysts. Elemental segregation occurs both on the surface and in the interior of the nanoparticles. The surface layer consists mainly of Pt atoms, forming (100), (110) and (111) planes and a small fraction of high-index facets. Using the experimental 3D coordinates, we quantitatively characterized the surface concaveness, structural and chemical order/disorder, coordination number (CN) and surface bond length of the nanocatalysts (Methods). Although the majority of the nanoparticles exhibit an octahedral morphology, we observed varying degrees of surface concaveness, structural disorder and chemical disorder in all of these nanocatalysts (Fig. 2a–c, respectively). We found that the Mo dopants increase the surface concaveness and the structural disorder, while preserving more subsurface Ni atoms (Fig. 2a,b,d, respectively). The CN of the surface Pt sites ranges from 4 to 11 with a peak at CN = 9 (Fig. 2e). The average surface Pt–Pt bond length was measured to be 2.77 ± 0.16 Å for PtNi and 2.75 ± 0.19 Å for Mo-PtNi (Fig. 2f), which correlates with the subsurface Ni composition. An increase in the subsurface Ni composition reduces the average surface Pt–Pt bond length (Fig. 2g).

To examine how catalytic activation changes the structure and composition of the nanocatalysts, we used AET to determine the 3D atomic structures of six PtNi and Mo-PtNi nanocatalysts before catalytic activation (Supplementary Fig. 10). We then compared these with the 3D atomic structures of the 11 PtNi and Mo-PtNi nanocatalysts after activation. We observed that the activation process changes the surface Pt–Pt bond length, the nearest-neighbour Pt and Ni atoms of each surface Pt atom and the average surface and subsurface Ni composition. In particular, the decrease in the surface and subsurface Ni concentration after catalytic activation indicates that the activation process leaches more Ni than Pt atoms from both the surface and subsurface (Supplementary Fig. 11), which is consistent with other experimental observations[40–42]. We also found a correlation between the subsurface Ni composition and the surface Pt–Pt bond length (Supplementary Fig. 11f). As the subsurface Ni composition increases, the average surface Pt–Pt bond length decreases in the nanocatalysts, indicating that subsurface Ni induces compressive strain of the surface Pt sites. These experimental results demonstrate that AET is an effective tool for capturing the 3D structural and compositional changes of PtNi and Mo-PtNi nanocatalysts upon catalytic activation.

Identifying the active sites of Pt alloy nanocatalysts

The experimentally determined 3D atomic coordinates were used with DFT-trained ML to identify the ORR active sites of the nanocatalysts (Methods). This approach represents an important advance over previous studies that only combined ML and DFT to predict the activity of electrocatalysts[43,44]. The ORR primarily occurs through a four-step electroreduction mechanism: $O_2 + 4(H^+ + e^-) \rightarrow 2H_2O$ (Methods), in which the surface hydroxyl group (OH) is an intermediate[14]. DFT calculations have revealed that the ORR activity follows the Sabatier principle[11,14,45], which states that optimal catalysts have an adsorption energy for the intermediates that is neither too strong nor too weak. The optimal ORR activity occurs when the OH binding energy (BE_{OH}) is about 0.13 eV weaker than that on the surface of Pt(111)[11,14]. As it is computationally impractical to perform DFT calculations for all 11 nanocatalysts, each containing several thousand to over ten thousand atoms, we adapted a DFT-trained ML method. Using 3D atomic models of PtNi and DFT-calculated OH binding energies, we predicted the OH binding energies on all of the surface Pt sites of the experimentally determined nanoparticles (Methods). We first constructed 292 PtNi atomic models, each with different 3D arrangements of Pt and Ni atoms, and adsorbed OH on a surface Pt site in each case (Supplementary Fig. 12). After calculating the BE_{OH} for the 292 Pt sites via DFT, we randomly selected 195 sites to train the ML method. We then used the trained method to identify the BE_{OH} of the remaining 97 test Pt sites. A quantitative comparison between the DFT-calculated and ML-identified BE_{OH} data is shown in Supplementary Fig. 13. This comparison indicates that the ML method accurately predicted the BE_{OH} with a root mean squared error (RMSE) of 0.05 per site for the 195 training sites and 0.07 eV per site for the 97 test Pt sites.

After training and validating the ML method, we applied it to evaluate the ORR activity for the experimentally measured surface Pt sites of the PtNi and Mo-PtNi nanocatalysts after catalytic activation.

Fig. 1 | 3D atomic structure of four representative nanocatalysts determined by AET. a–h, 3D surface morphology and chemical composition (**a**), elemental segregation in the interior (**b**), facets (**c**), surface concaveness (**d**), structural order/disorder (**e**), chemical order/disorder (**f**), CN of the surface Pt sites (**g**) and surface bonds (**h**) of the nanocatalysts after activation, which were quantitatively characterized using the experimental atomic coordinates. For the structural order, a bond orientational order (BOO) of 1 corresponds to a perfect face-centred cubic (fcc) lattice. For the chemical order, positive and negative numbers represent segregation and alloying, respectively. From left to right, the four nanocatalysts correspond to particles 1–4, respectively, in Supplementary Table 2. Scale bar, 2 nm.

https://doi.org/10.1038/s41929-024-01175-8

We focused on the activity of the nanoparticles after activation because the 3D morphology and structure of the nanoparticles before activation were modified by the ORR test performed in 0.1 M $HClO_4$ (ref. 40). By comparing BE_{OH} with the reference OH binding energy of Pt(111) (ref. 14), we obtained the ORR activity for 17,985 surface Pt sites (Methods). The average specific activities of the 11 nanocatalysts

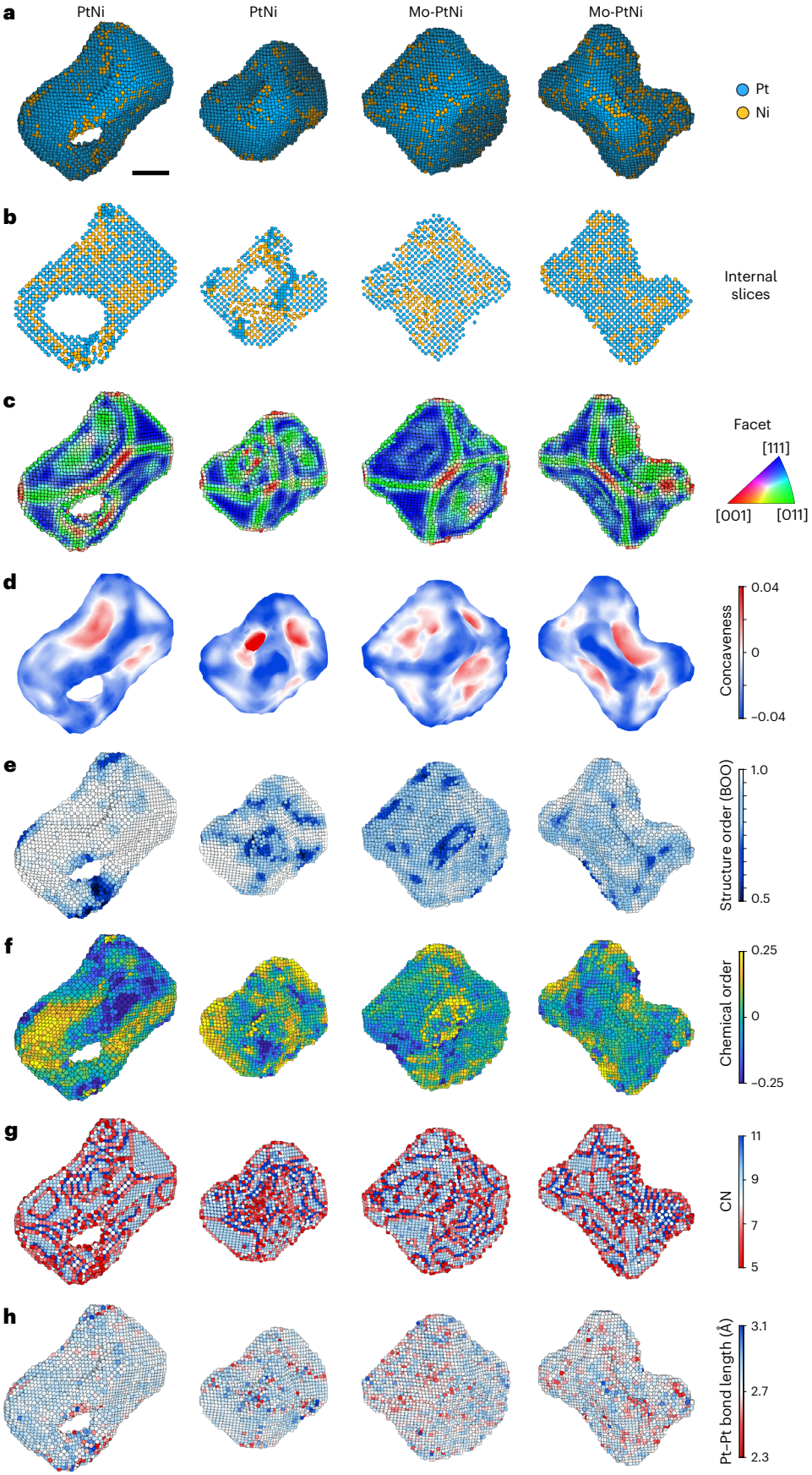

https://doi.org/10.1038/s41929-024-01175-8

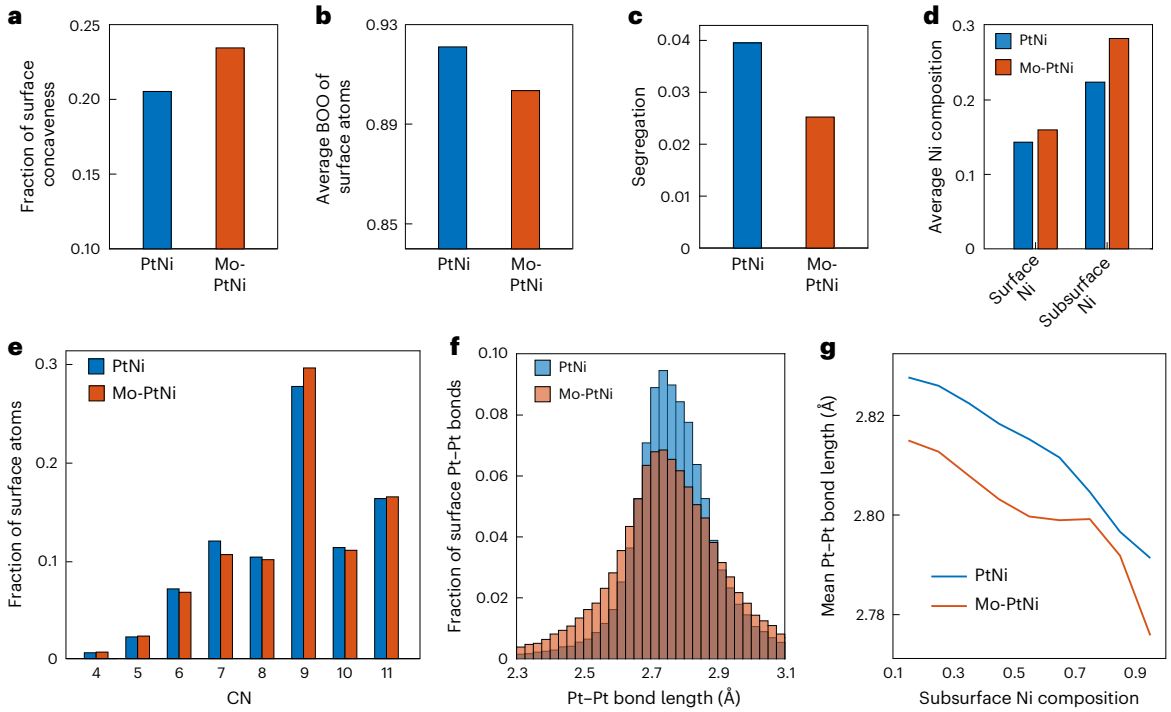

Fig. 2 | Atomic-scale characterization of PtNi and Mo-PtNi nanocatalysts after activation. a, Histogram of the fraction of atoms with surface concaveness. **b**, The average BOO distribution of the surface atoms, where BOO = 1 corresponds to a perfect fcc lattice. **c**, The fraction of surface segregation. **d**, Histogram of average surface and subsurface (that is, the layer below the surface) Ni composition. **e**, Distribution of the CN of the surface Pt sites. **f**, Distribution of the surface Pt–Pt bond length. **g**, Correlation between the subsurface Ni composition and the surface Pt–Pt bond length.

agreed well with the electrochemical measurements (Methods; Fig. 3a and Supplementary Table 3), demonstrating the validity of using DFT-trained ML to identify the ORR activity for the experimental 3D atomic coordinates. Figure 3b,c, Supplementary Video 2 and Supplementary Fig. 14 show the ORR activity maps of the surface Pt sites for the 11 PtNi and Mo-PtNi nanocatalysts. We observed that the ORR activity of the surface Pt sites varies by several orders of magnitude. While the majority of the surface Pt sites have low catalytic activity, there is a very small fraction of highly active sites (yellow atoms in Fig. 3b,c and Supplementary Fig. 14). Figure 3d–i shows six representative highly active sites on the PtNi and Mo-PtNi nanocatalysts, each exhibiting a distinct 3D local environment, such as a different CN, neighbouring Ni atoms and surface morphology. This observation indicates that quantitative characterization of the 3D local atomic environment is critical for understanding the active sites of nanocatalysts.

The local environment descriptor

To gain quantitative insights into the ORR active sites of the nanocatalysts, we conducted a comprehensive analysis of the structure–activity relationship at the individual atom level. We fitted a large number of experimentally measured structural and chemical properties, such as the surface concaveness, CN, Pt–Pt bond length, structure and chemical order parameters, strain/ligand effects, among others, to the BE_{OH} values of the 17,985 surface Pt sites of the PtNi and Mo-PtNi nanocatalysts (Methods). By minimizing the RMSE between the calculated and ML-determined BE_{OH}, we derived the local environment descriptor (LED) (Supplementary Table 4), which relates the catalytic activity of each active site to the local 3D arrangement of its surrounding Ni and Pt atoms,

$$\mathrm{LED} = \mathrm{NN}^{\mathrm{Pt}} \times e^{-a_1\varepsilon} + a_2 \times \overline{\mathrm{CN}}^{\mathrm{Ni}}, \quad (1)$$

where $\mathrm{NN}^{\mathrm{Pt}}$ is the number of nearest-neighbour Pt atoms of a surface Pt site; $\varepsilon = \frac{\bar{d}_{\mathrm{Pt}} - d_0}{d_0}$ is the local strain, where $\bar{d}_{\mathrm{Pt}}$ is the average Pt–Pt bond length around the surface Pt site and d_0 is the Pt–Pt bond length (2.75 Å) for Pt nanocrystals; $\overline{\mathrm{CN}}^{\mathrm{Ni}} = \sum_i \frac{\mathrm{CN}_i^{\mathrm{Ni}}}{\mathrm{CN}_{\max}}$ is the generalized CN of the considered Pt with Ni atoms[11,46], where $\mathrm{CN}_i^{\mathrm{Ni}}$ is the CN of the i^{th} Ni atom and $\mathrm{CN}_{\max}$ (= 12) is the CN in bulk Pt; a_1 and a_2 are two fitting constants related to the strain and ligand effects, respectively. Our quantitative analysis showed that $\mathrm{NN}^{\mathrm{Pt}}$, $\bar{d}_{\mathrm{Pt}}$ and $\overline{\mathrm{CN}}^{\mathrm{Ni}}$ are more relevant to the ORR activity of the nanocatalysts than other properties such as the surface concaveness and structural and chemical order/disorder (Methods and Supplementary Table 4). By fitting the LED to the BE_{OH} of the 17,985 surface Pt sites relative to the OH binding energy of Pt(111), we obtained the distribution of the ORR activity as a function of the LED. This resulted in a volcano plot with the peak at LED = 10.02 (dashed red line in Fig. 3j). The RMSE of the fitting is 0.104 eV with $a_1 = 2.13$ and $a_2 = 1.14$. The small RMSE value indicates the robustness of the structure–activity fitting analysis. Figure 3k,l, Supplementary Fig. 15 and Supplementary Video 2 show the activity maps of the 11 PtNi and Mo-PtNi nanocatalysts based on the LED, which agree well with the ML-identified activity maps (Fig. 3b,c and Supplementary Fig. 14). As specific examples, the six highly active sites shown in Fig. 3d–i have their LED value close to the peak of the volcano plot.

To further validate the LED, we considered Pt(111) surface sites without strain. Using equation (1), we calculated an LED value of 9, which is located on the left-hand side of the peak of the volcano plot (Fig. 3j). If a nearest-neighbour surface Pt atom is substituted by a Ni atom, the first term of equation (1) decreases by 1, while the second term increases by a number smaller than 1. This makes LED smaller than 9, thereby decreasing the catalytic activity (Fig. 3m). If the substitutional Ni atom is in the subsurface, the CN of the Ni atom is 12, and the second term increases by a value larger than 1 since $a_2 > 1$, making the LED larger than 9 (Fig. 3n). Furthermore, compressive strain, induced by a decrease in the average Pt–Pt bond length, also increases the LED (Fig. 3o). Consequently, with LED < 10.02, both subsurface Ni atoms and compressive strain increase the ORR

https://doi.org/10.1038/s41929-024-01175-8

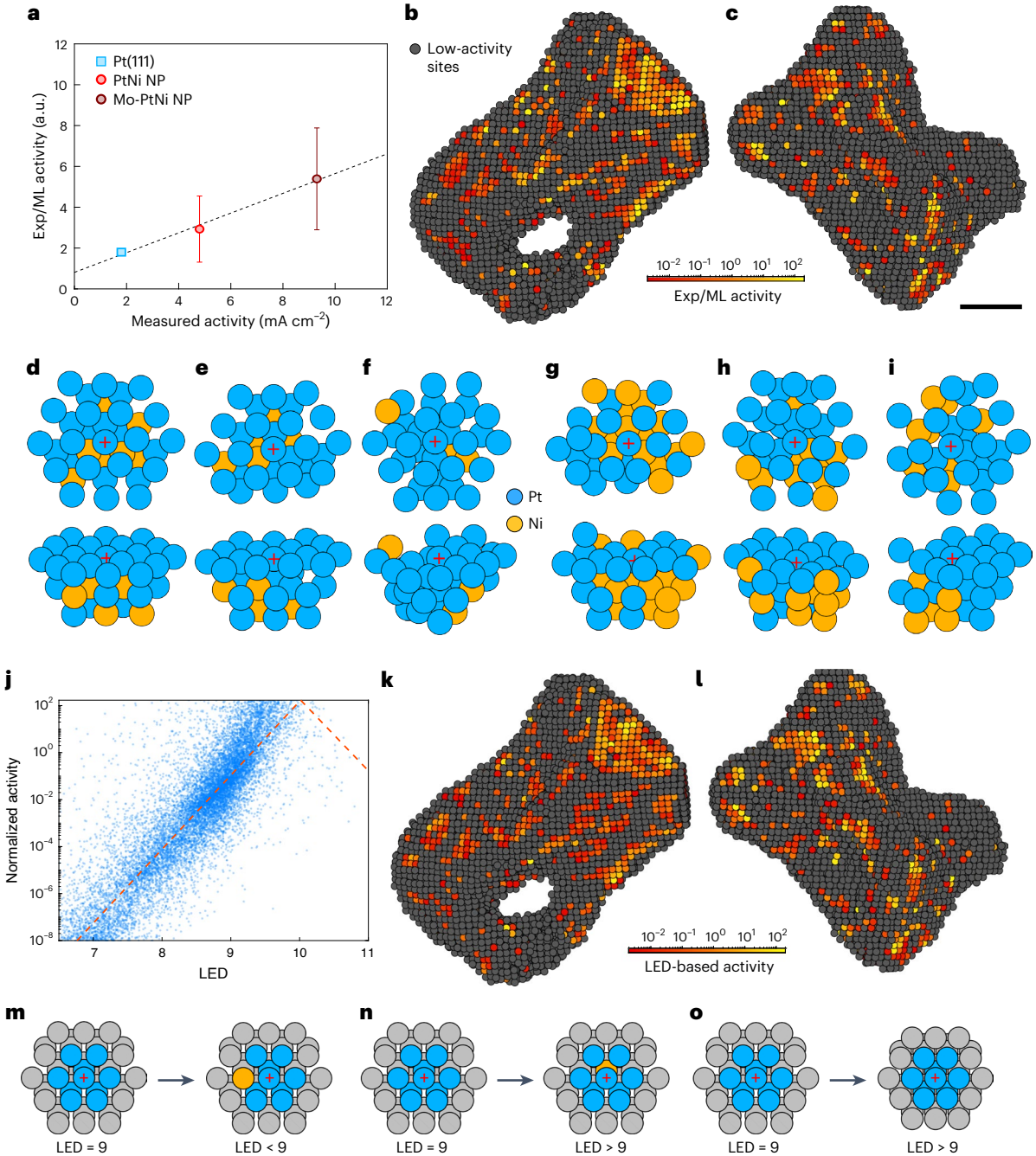

Fig. 3 | Identification of the active sites of the nanocatalysts. a, Comparison between the specific activity at 0.9 V_{RHE} and the ML-identified activity for the experimental 3D atomic coordinates of 11 PtNi and Mo-PtNi nanocatalysts after activation. The mean and standard deviation values are shown as circles and error bars, respectively. The activity of Pt(111) was obtained from ref. 4 and also used in DFT as a reference point for our simulations.[4] NP, nanoparticle; Exp, experimental. **b**,**c**, The ML-identified activity maps for the experimental 3D atomic coordinates of a PtNi (**b**) and a Mo-PtNi (**c**) nanocatalyst, which correspond to particles 1 and 4, respectively. Low-activity sites are defined as having an ORR activity smaller than 3% of that of Pt(111). Scale bar, 2 nm. **d**–**i**, Six representative highly active sites (denoted by the red crosses) on the PtNi (**d**–**f**) and Mo-PtNi (**g**–**i**) nanocatalysts, each with an ORR activity more than 120 times higher than that of Pt(111). The top and bottom rows show the plan and side views, respectively, of the six active sites. For **d**–**i**, the LED values are 9.96, 9.97, 10.19, 10.18, 9.94 and 9.96, respectively. **j**, Volcano-type activity plot (red dashed line) obtained by fitting the LED with the ML-identified activity of all the surface Pt sites (blue dots), with the peak at LED = 10.02. **k**,**l**, LED-based activity maps of the PtNi (**k**) and Mo-PtNi (**l**) nanocatalysts (particles 1 and 4, respectively), which are in good agreement with the ML-identified activity maps (**b** and **c**). For Pt(111) surface sites without strain, according to equation (1), LED = 9 (Methods). **m**, The substitution of a surface Pt atom by a Ni atom reduces the LED and the catalytic activity. **n**, The substitution of a subsurface Pt atom by a Ni atom increases the LED and the catalytic activity. **o**, Compressive strain also increases the LED and the catalytic activity.

activity. However, when the LED reaches the peak of the volcano plot (LED = 10.02 in Fig. 3j), further increases in subsurface Ni atoms and compressive strain reduce the ORR activity. Thus, the LED quantitatively balances the strain and ligand effects to optimize the ORR activity of PtNi and Mo-PtNi nanocatalysts. To further examine the LED, we applied it to pure Pt nanocatalysts, using only the first term of equation (1) as the second term becomes 0. By comparing the results with the DFT-calculated BE_{OH}, we found that the LED outperforms the

generalized CN both with and without the consideration of strain[11,47] (Supplementary Fig. 16).

The LED can also be used to better understand the experimental results of Pt alloy nanocatalysts. Our experimental data revealed that Mo-PtNi has a shorter surface Pt–Pt bond length and a broader distribution than PtNi (Fig. 2f), indicating that Mo-PtNi experiences larger compressive strain than PtNi. In addition, Mo-PtNi retains more subsurface Ni atoms than PtNi (Fig. 2d). According to equation (1), both factors increase the LED of Mo-PtNi compared to PtNi. As the measured and the ML-identified ORR activity values of Mo-PtNi are higher than those of PtNi (Fig. 3a), our observations indicate that the average catalytic activity of the Mo-PtNi and PtNi nanocatalysts is situated on the left-hand side of the peak in the volcano plot (Fig. 3j). This can explain previous experimental results where a higher concentration of Co or Ni in Pt alloy nanocatalysts increases the ORR activity[48,49]. Although we focused on PtNi and Mo-PtNi nanocatalysts in this study, our approach for constructing the LED can be applied to investigate other nanocatalysts and reactions.

Conclusions

In summary, we determined the 3D local atomic structure and chemical composition of PtNi and Mo-PtNi nanocatalysts, each consisting of several thousand to over ten thousand atoms. We measured the facets, surface concaveness, structural and chemical order/disorder, CN and bond lengths in 3D atomic detail. We revealed that the Mo-PtNi nanocatalysts have larger surface concaveness, more structural disorder, a smaller surface Pt–Pt bond length, a wider Pt–Pt bond length distribution and a greater subsurface Ni composition compared to the PtNi nanocatalysts. Furthermore, from the experimental 3D atomic coordinates, we used a DFT-trained ML method to identify the active sites of the 11 nanocatalysts, which were validated through electrochemical measurements. By performing a comprehensive analysis of the structure–activity relationship, we derived the LED to quantitatively characterize the ORR activity of the nanocatalysts based on their surface, subsurface atomic structure and chemical composition. We found that the nearest-neighbour surface Pt atoms (N_{Ni}^{Pt}), the local strain (ε) and the generalized CN for Ni neighbours ($\overline{CN}^{Ni}$) are the most relevant parameters for the ORR activity. Compressive strain on the surface Pt–Pt bond and subsurface Ni atoms enhance the ORR activity, whereas the surface Ni atoms hinder the activity. The optimal reactivity is achieved with the correct balance between the strain and ligand effects. We expect that this work paves the way for measuring the 3D local atomic positions, chemical species, and surface composition of a wide range of nanocatalysts for various (electro)chemical reactions and for correlating the 3D atomic structure with the catalytic activity at the single-atom level.

Methods

Chemicals and materials

Platinum(II) acetylacetonate ($Pt(acac)_2$), nickel(II) acetate tetrahydrate [$Ni(ac)_2{\cdot}4H_2O$], benzoic acid were purchased from Sigma Aldrich. Molybdenum hexacarbonyl ($Mo(CO)_6$) and carbon nanotubes were purchased from Alfa Aesar. *N*,*N*-Dimethylformamide (DMF), acetone and isopropanol were purchased from Fisher Scientific. Ethanol was purchased from Decon Laboratories. Vulcan XC-72 carbon black (particle size, ~50 nm) was obtained from Cabot Corporation. Water used in the experiments was obtained from an Millipore ultrapure water system (18.2 MΩ cm).

Sample preparation

Vulcan XC-72 carbon black was pretreated in an argon (80% by volume) and hydrogen (20% by volume) mixture at 400 °C for 4 h. Pretreated Vulcan XC-72 carbon black (80 mg) was dispersed in DMF (60 ml) under ultrasonication for 30 min in a 325 ml pressure bottle. Then, $Pt(acac)_2$ (64 mg), $Ni(ac)_2{\cdot}4H_2O$ (32 mg) and benzoic acid (520 mg) were dissolved in DMF (10 ml), and this mixture was also added to the 325 ml pressure bottle containing the carbon black dispersion. After ultrasonication for 5 min, the pressure bottle with the well-mixed solution was placed directly in an oil bath at 140 °C and heated slowly to 160 °C over a period of 2 h. The pressure bottle was kept at 160 °C for 12 h. After 12 h, $Pt(acac)_2$ (16 mg), $Ni(ac)_2{\cdot}4H_2O$ (8 mg) and $Mo(CO)_6$ (3.2 mg) were added to the pressure bottle. Then the pressure bottle was kept in the 160 °C oil bath for 48 h. After the reaction had finished, the catalysts were collected via centrifugation, then dispersed and washed with an isopropanol and acetone mixture. The catalysts were then dried under vacuum at room temperature, after which they were ready for characterization and electrochemical testing.

The synthesis procedure for PtNi/C is same as that noted above for Mo-PtNi/C but without the addition of $Mo(CO)_6$. The synthesis procedure for the PtNi/CNT and Mo-PtNi/CNT samples is same as for PtNi/C and Mo-PtNi/C noted above apart from the pretreated Vulcan XC-72 being replaced with carbon nanotubes.

Electrochemical measurements and analysis

A typical catalyst ink was prepared by mixing catalyst powder (Mo-PtNi/C, PtNi/C; 2.8 mg) with a 2 ml volume of ethanol solution containing Nafion (16 µl; 5 wt%) with ultrasonication for 5 min. Then, the catalyst ink (10 µl) was added dropwise on to a 5-mm-diameter glassy-carbon electrode (Pine Research Instrumentation). The Pt loading was estimated based on the overall Pt ratio within the catalyst, determined using inductively coupled plasma atomic emission spectroscopy (Supplementary Table 5). The ink was dried under an infrared lamp; the electrode was then ready for electrochemical testing.

A three-electrode cell was used to carry out the electrochemical measurements: the working electrode was a catalyst-coated glassy-carbon electrode; a Ag/AgCl electrode was used as the reference electrode; and a Pt wire (diameter, 0.05 cm; length, 23 cm) was used as the counter electrode. The geometric exposed surface area of the counter electrode (A_{CE}) was around 3.6 cm^2, which is more than 18 times that of working electrode (A_{WE}; 0.196 cm^2). The high A_{CE}/A_{WE} ratio was chosen to eliminate Pt dissolution at the counter electrode. The catalytic activation procedure was conducted using the cyclic voltammetry process in a N_2-saturated 0.1 M $HClO_4$ solution between 0.05 and 1.1 V versus the reversible hydrogen electrode (RHE) at a sweep rate of 100 mV s^{-1} for 30 cycles. The ORR measurements were conducted in an O_2-saturated 0.1 M $HClO_4$ solution at a sweep rate of 20 mV s^{-1}. Both iR compensation (i, current; R, resistance) and background subtraction were applied for the ORR test curves following the protocol noted in the literature[50]. For the ORR measurement without catalytic activation, the prepared working electrode was directly subjected to ORR testing in the O_2-saturated electrolyte without being activated at the N_2-saturated electrolyte via cyclic voltammetry scanning.

The specific activity is defined as the estimated kinetic current (at 0.9 V versus RHE) divided by the measured active surface area. The mass activity is the estimated kinetic current (at 0.9 V versus RHE) divided by the total Pt mass loaded on the working electrode. The electrochemically active surface area refers to the measured active surface area normalized by the total Pt mass loaded on the working electrode.

Data acquisition

The PtNi and Mo-PtNi nanocatalysts with a CNT matrix were deposited on to 6-nm-thick silicon nitride membranes (Norcada; chip size 3 mm, window size 1.8 mm × 30 µm). Tomographic tilt series were acquired from several nanoparticles using the transmission electron aberration-corrected microscope at the National Center for Electron Microscopy, Lawrence Berkeley National Laboratory. The tilt range and angular increments of the nanoparticles are provided in Supplementary Table 2. At each tilt angle, high-resolution images were collected at 300 kV in ADF-STEM mode. To minimize sample drift, three to five

images per angle were measured with a 3 µs dwell time. To ensure that no structural changes were observed during the data acquisition, for each nanoparticle, we took the same projection images at zero degrees before, during and after the acquisition of each tilt series. A total of nine PtNi and eight Mo-PtNi nanoparticles with a CNT matrix were measured in this work. The total electron dose of each tilt series for all of the nanoparticles was estimated to be between 7.4×10^5 and 8.5×10^5 $e^- Å^{-2}$ (Supplementary Table 2).

Image registration and drift correction

The three to five ADF-STEM images acquired at each tilt angle were registered using a cross-correlation algorithm. Adopting the first image as a reference, we scanned a cropped region of the subsequent images with a subpixel step size and found the drift for every image. The drift of the sample holder/stage could make the pixel shape not square due to distortion. The angle of the parallelogram pixel is correlated with the drift rate, which can be calculated via registration of consecutive images. After drift correction, we averaged all of the images at each angle.

Image denoising

The experimental ADF-STEM images have mixed Poisson and Gaussian noise. A generalized denoising algorithm, termed block matching and 3D filtering, was used to denoise each averaged image[51]. The robustness of block matching and 3D filtering on the AET data has been proved in our previous studies[34–36,52].

Image alignment and background subtraction

The denoised images of each tilt series were aligned by the centre of mass and common line method as described elsewhere[33,53]. After alignment, a two-dimensional mask was calculated via the Otsu threshold in MATLAB for each image to match the shape of the nanoparticle[54]. The background was estimated using the discrete Laplacian function in MATLAB. After background subtraction, all of the images in each tilt series were re-aligned by the centre of mass and common line to further reduce the error.

3D image reconstruction and refinement

After image preprocessing, each tilt series was reconstructed using an iterative algorithm, termed REal Space Iterative REconstruction (RESIRE)[55]. From the experimental images, RESIRE minimized the L_2-norm error metric using gradient descent. The jth iteration of the algorithm consists of the following steps. RESIRE computed a set of images from the 3D object of the $(j-1)$th iteration. The difference between the computed and corresponding experimental images was calculated, from which an error metric was defined to monitor the convergence of the algorithm. The difference was back-projected to real space, yielding the gradient of the 3D reconstruction. The 3D reconstruction of the jth iteration was updated by combining the gradient with the reconstruction of the $(j-1)$th iteration, where positivity was enforced as a constraint. As a general algorithm, RESIRE is not sensitive to the initial input. After 200 iterations, a preliminary 3D reconstruction was computed. Based on the preliminary 3D reconstruction, angular refinement and spatial alignment were performed and background subtraction was re-evaluated. After these refinement procedures, a final 3D reconstruction was obtained by running 200 iterations of RESIRE.

Determination of 3D atomic coordinates and chemical species

To increase the precision of atom tracing, we oversampled each 3D reconstruction by a factor of three using spline interpolation. The local maxima were identified by tracing the local peak positions of the oversampled 3D reconstruction. Starting from the highest intensity, we fitted each local maximum of a $9 \times 9 \times 9$ voxel volume ($1.4 \times 1.4 \times 1.4$ Å) via a 3D polynomial method to locate its centre position[52]. Each fitted local maximum was considered as a potential atom only when its distance from the existing potential atoms was larger than 2 Å. After going through all of the local maxima, we obtained a list of potential atoms. For every potential atom, the integrated intensity of the $9 \times 9 \times 9$ voxel volume around the centre position was calculated. Supplementary Fig. 17 shows the average 3D intensity distribution of Ni and Pt atoms. A k-means clustering method was used to classify the non-atoms, Pt and Ni atoms[35]. Owing to a very small fraction (~0.4%) of Mo atoms in the Mo-PtNi nanoparticles, AET is currently not sensitive enough to distinguish them from Pt or Ni atoms. After excluding the non-atoms and manually checking all of the atoms, we obtained an initial 3D atomic model for each 3D reconstruction.

Owing to the missing-wedge problem[33,53], we used local re-classification to reduce the effect of the intensity variation in different regions of each 3D reconstruction[52]. At each atomic position, we cropped a 7 Å radius sphere and calculated the mean integrated intensity for the Pt or Ni atom inside the sphere. We then re-classified each atom in the sphere on the basis of the difference between its integrated intensity and the mean value of the Pt or Ni atom. The procedure was repeated until there was no further change.

The electron energy-loss spectroscopy maps of the nanoparticles show that there are individual Ni atoms distributed around each nanoparticle (Supplementary Fig. 2). To evaluate the effect of the surrounding Ni atoms on the 3D reconstruction, we simulated a PtNi atomic model in an environment with individual Ni atoms. We randomly positioned Ni atoms around the experimentally determined 3D atomic model to match the Ni concentration in the background of the electron energy-loss spectroscopy maps (Supplementary Fig. 2c,d). After calculating projection images at different tilt angles from the model[52], we performed image preprocessing, carried out the 3D reconstruction, traced the atoms, classified the atomic species and obtained a new 3D atomic model (Supplementary Fig. 8). We observed that there is a layer of ghost atoms surrounding the 3D atomic model, which is due to the surrounding Ni atoms around each nanoparticle (Supplementary Fig. 8d,e). Based on this result, a layer of ghost atoms was removed from the experimental 3D atomic model of each nanoparticle.

X-ray absorption spectroscopy data collection and analysis

XAS experiments were conducted on the dry powder samples of the nanocatalysts studied in this work at beamline 8-ID (ISS) of the National Synchrotron Light Source II (Brookhaven National Laboratory, New York). Full-range Pt L_3-edge and Ni K-edge spectra were collected on the same electrode in transmission mode at the Pt L_3 edge and/or Ni K edge, with a Pt or Ni reference foil positioned between two ion chambers (I2 in the front and I3 behind) as a reference. Typical experimental procedures were utilized with details provided in our previous work[56]. The data were processed and fitted using the IFEFFIT-based Athena[57] and Artemis[58] programs. Scans were calibrated, aligned and normalized with the background removed using the IFEFFIT suite[59]. The χ(R) were modelled using single scattering paths calculated using the FEFF6 program, where χ(R) represents the Fourier transform in the R space[60].

The Pt–Pt bond lengths of the nanocatalysts were obtained via EXAFS fitting (Supplementary Figs. 18 and 19 and Supplementary Table 6). The average first-shell Pt–Pt bond lengths were determined by fitting the EXAFS spectra of dry powder samples at the Pt L_3 and Ni K edge simultaneously. S_0^2 represents the amplitude reduction factor and was fixed at 0.84 and 0.68 for Pt and Ni, respectively, as obtained by fitting the reference foils. Fits were carried out in R-space, $k^{1,2,3}$ weighting: $1.2 < R < 3.1$ Å and $\Delta k = 3.08–13.39$ $Å^{-1}$ were used for fitting the Pt L_3-edge data; $1.3 < R < 3.1$ Å and $\Delta k = 2.56–11.40$ $Å^{-1}$ were used for fitting the Ni K-edge data. The fitting results of the variable E_0 at the Pt L_3 and Ni K edges are 8 ± 2 eV and -6 ± 1 eV, respectively. The EXAFS fit Pt–Pt bond lengths were used to calibrate the voxel size of the AET experiment.

Calculation of the CN, facet orientation and surface concaveness

We used custom MATLAB scripts to measure the CN, facet orientation and surface concaveness for all of the atomic sites. We defined the nearest-neighbour distance by fitting the valley of the first and second peak of the pair distribution function for each nanocatalyst, which was calculated from the experimental 3D atomic models using a method described elsewhere[35]. The CN was obtained by counting the number of nearest-neighbour sites within the cut-off distance. Each atom was classified as a surface site if CN < 12 and as an internal site if CN = 12. To find the facet orientation, we derived a density matrix for each nanocatalyst by convolving the atomic structure with a 3D Gaussian function (σ = 4 Å). For each surface site, a normal vector was calculated by computing the gradient of the density matrix at that site. By comparing the normal vectors with the crystallographic directions, we determined the facet orientation of the nanocatalyst. To quantify the surface concaveness, we estimated the surface curvature for all of the surface sites using a procedure published elsewhere[61].

The normalized local BOO parameter

From the 3D atomic model of each nanoparticle, we calculated the local BOO parameters (Q_4 and Q_6), which are described elsewhere[35,62]. The Q_4 and Q_6 order parameters were computed up to the second shell with a shell radius of 3.5 Å. We then defined the normalized local BOO parameter as $\sqrt{{Q_4}^2 + {Q_6}^2}/\sqrt{Q_{4\,\mathrm{fcc}}^2 + Q_{6\,\mathrm{fcc}}^2}$, where $Q_{4\,\mathrm{fcc}}$ and $Q_{6\,\mathrm{fcc}}$ are the Q_4 and Q_6 values of a perfect fcc lattice, respectively. The normalized BOO parameter is between 0 and 1, where 0 means that $Q_4 = Q_6 = 0$, and 1 represents a perfect fcc crystal structure.

The chemical order parameter

The chemical order of each nanoparticle was calculated via the pair-wise multicomponent short-range order parameter[63],

$$\alpha_{ij} = \frac{p_{ij} - C_j}{\delta_{ij} - C_j} \tag{2}$$

where p_{ij} is the probability of finding a j-type atom around an i-type atom in the first nearest-neighbour shell, C_j is the concentration of j-type atoms in the nanoparticle and δ_{ij} is the Kronecker delta function. As there are primarily Pt and Ni atoms in the nanoparticles, all of the α_{ij} parameters are correlated. In this study, we chose α_{12} to represent the chemical order parameter. A positive and a negative α_{12} represent segregation and alloying, respectively.

DFT calculations

The structure optimizations were carried out using LCAO mode in the GPAW package[64,65], and refined using the VASP package[66–71]. In the VASP calculations, the core electrons were described by the projector augmented-wave method[72] and the valence states by plane waves up to 400 eV. The exchange–correlation interaction of electrons was defined via the Perdew–Bruke–Ernzerhof functional[73]. Spin-polarized calculations were used throughout this manuscript for the PtNi nanocatalysts. The Brillouin zone was sampled by a uniform density of 0.19 Å^{-1} in each reciprocal direction. For isolated clusters, only the Γ point was considered. The ORR reaction mechanism can be summarized by the following four equations:

$$O_2(g) + H^+ + e^- \rightarrow OOH^* \tag{3}$$

$$OOH^* + H^+ + e^- \rightarrow O^* + H_2O(l) \tag{4}$$

$$O^* + H^+ + e^- \rightarrow OH^* \tag{5}$$

$$OH^* + H^+ + e^- \rightarrow H_2O(l). \tag{6}$$

The binding energies for the adsorbed hydroperoxyl (OOH*), oxygen (O*) and hydroxyl (OH*) radicals were correlated linearly among different metals[14]. This enabled us to use the OH adsorption energy as the descriptor of the ORR reactivity. A database of OH adsorption energies on the surface Pt sites of the PtNi model catalysts were computed by DFT (Supplementary Fig. 12). The database includes diverse 3D atomic models that consist of nanoclusters and slabs. The nanoclusters of different sizes were built from truncated octahedra, and the slab models were created from close-packing surfaces, including fcc(110) surfaces, fcc(100) surfaces and concave shapes similar to these published elsewhere[11]. Ni atoms were introduced by randomly replacing the Pt atoms. The Ni concentration ranged from 0 to 69.6% in the 3D atomic models and from 0 to 83.9% in the local environment (defined as the atoms within the 6.5 Å radius of an adsorption site). Different lattice constants were used to represent tensile and compressive strain. In total, OH was adsorbed on 292 Pt sites with different Pt CN, Ni concentration and local environments. The OH binding energy on the Pt sites (BE_{OH}) was computed via

$$BE_{OH} = E_{OH@model} - E_{OH} - E_{model} \tag{7}$$

where $E_{OH@model}$ is the total electronic energy of the optimized OH adsorbed structure, E_{OH} is the electronic energy of the OH radical in the gas phase and E_{model} is the energy of optimized model without OH adsorption.

Evaluation of the OH binding energy using DFT-trained ML

We used a ML method—the Gaussian process regression (GPR)[74]—to evaluate BE_{OH} for all of the surface Pt sites of the experimentally determined nanocatalysts. We constructed 292 PtNi atomic models and calculated the BE_{OH} for the 292 Pt sites using DFT, and these were used as input to train the ML-GPR model. The trained model was then applied to predict the BE_{OH} of different Pt surface sites based purely on geometric information, for example, the local environment of the considered Pt sites. The local atomic environment of the Pt sites was characterized using the smooth overlap of atomic positions (SOAP) approach[75,76]. The cut-off radius of 6.5 Å was selected for the SOAP approach, which was later validated via the accurate prediction of the ML-GPR method (Supplementary Fig. 13). The ML-GPR method finds a correlation between the local environment (characterized by SOAP) and the DFT-calculated BE_{OH}. The GPR was implemented by the Python-scikit package[77]. The kernel function is defined as normalized polynomial kernel of the partial power spectrum,

$$K(\mathbf{d}_1, \mathbf{d}_2) = \left(\frac{\mathbf{d}_1^{\mathrm{T}} \mathbf{d}_2}{\sqrt{\mathbf{d}_1^{\mathrm{T}} \mathbf{d}_1 \mathbf{d}_2^{\mathrm{T}} \mathbf{d}_2}} \right)^{\zeta} \tag{8}$$

where $K(\mathbf{d}_1, \mathbf{d}_2)$ is the kernel function between SOAP descriptors $\mathbf{d}_1$ and $\mathbf{d}_2$, and ζ is a hyperparameter. In this study, we chose $\zeta = 4$ by balancing the accuracy and transferability. We trained the GPR by randomly choosing 195 atomic models and then used the ML method to predict the BE_{OH} of the remaining 97 atomic models. The RMSE is 0.05 and 0.07 eV per site for the training and test sets, respectively (Supplementary Fig. 13). The small RMSE values indicate the robustness of the ML method. After validating DFT-trained ML, we applied it to evaluate the BE_{OH} of the surface Pt sites of the seven PtNi nanocatalysts and the four Mo-PtNi nanocatalysts.

Estimation of the ORR activity based on the OH binding energy

From the ML-identified BE_{OH}, we estimated the ORR activity of 17,985 surface Pt sites with CN < 10. We did not choose the sites with CN ≥ 10 because, according to the previous and our current DFT calculations[11], steric hindrance, weak adsorption energies and proximity to undercoordinated sites result in adsorbate diffusion to neighbouring sites. For the (111) surface sites, labelled as X(111), we calculated the ORR activity on the left and right side of the volcano plot using[78]

$$kT\ln\left(\frac{j_L}{j_{Pt(111)}}\right) = BE_{OH,X(111)} - BE_{OH,Pt(111)} \quad (9)$$

and

$$kT\ln\left(\frac{j_R}{j_{Pt(111)}}\right) = 0.26[eV] - 0.97 \times (BE_{OH,X(111)} - BE_{OH,Pt(111)}) \quad (10)$$

where k is Boltzmann constant, T is room temperature, j_L and j_R are, respectively, the current density on the left and right side of the volcano plot, $j_{Pt(111)}$ is the current density of Pt(111), and $BE_{OH,X(111)}$ and $BE_{OH,Pt(111)}$ are the OH binding energy of the X(111) sites and Pt(111), respectively. For the (100) surface sites X, labelled as X(100), we computed the ORR activity on the left and right side of the volcano plot using[78]

$$kT\ln\left(\frac{j_L}{j_{Pt(111)}}\right) = (BE_{OH,X(100)} - BE_{OH,Pt(100)}) - 0.15[eV] \quad (11)$$

and

$$kT\ln\left(\frac{j_R}{j_{Pt(111)}}\right) = 0.26[eV] + 0.15[eV] - 0.97 \times (BE_{OH,X(100)} - BE_{OH,Pt(100)}) \quad (12)$$

where $BE_{OH,X(100)}$ and $BE_{OH,Pt(100)}$ are the OH binding energy of the X(100) sites and Pt(100), respectively. Although other undercoordinated surface Pt sites on the experimental nanocatalysts may have different solvation energies from those of Pt(111) and Pt(100), the OH binding energies on those undercoordinated sites are too strong and thus negligible in evaluating the ORR activity. Figure 3b,c, Supplementary Fig. 12 and Supplementary Video 2 show the ML-identified activity of the 17,985 surface Pt sites (blue dots) for the seven PtNi and four Mo-PtNi nanocatalysts. We observed that the ORR activity of the various surface Pt atoms differs by several orders of magnitude. The average activity of these nanocatalysts is in good agreement with the electrochemically measured activity (Fig. 3a and Supplementary Table 3).

Derivation of the LED equation

We derived the LED by fitting a large number of experimentally measured structural and chemical properties to the BE_{OH} of the surface Pt sites of the seven PtNi and four Mo-PtNi nanocatalysts (Supplementary Table 4). The fitting variables include the CN, the surface CN, the subsurface CN, the average Pt–Pt bond length around each Pt site ($\overline{d}_{Pt}$), the structure/chemical order parameter, the nearest-neighbour Pt and Ni atoms of each surface Pt atom (NN^{Pt} and NN^{Ni}), the generalized CN ($\overline{CN}$), the element-based $\overline{CN}$ ($\overline{CN}^{Pt}$ and $\overline{CN}^{Ni}$) and so on. To avoid overfitting, we randomly chose 70% of the surface Pt sites (12,590) to derive the LED and the remaining 30% of the sites (5,935) as testing sites to validate the LED. Using the 12,590 sites, we fitted the LED to minimize the RMSE,

$$RMSE = \sqrt{\frac{\sum_{i=1}^{N}\left(BE_{OH,i}^{ML} - BE_{OH,i}^{cal}\right)^2}{N}} \quad (13)$$

where $BE_{OH,i}^{ML}$ is the BE_{OH} of the ith surface Pt site obtained by ML, N is the total number of the surface Pt sites and $BE_{OH,i}^{cal} = E_1 \times LED - E_0$, with E_1 and E_0 being two fitting constants. After fitting the variables, we derived an optimized equation, $LED = NN^{Pt} \times e^{-a_1\varepsilon} + a_2 \times \overline{CN}^{Ni}$, with the RMSE of 0.104 eV (Supplementary Table 4), where $\varepsilon = \frac{\overline{d}_{Pt} - d_0}{d_0}$, $d_0 = 2.75$ Å is the Pt–Pt bond length of the Pt nanoparticles, $a_1 = 2.13$, $a_2 = 1.14$, $E_1 = 0.19$ eV and $E_0 = 3.93$ eV. The RMSE of the LED for the 5,935 testing sites is 0.103 eV. The smaller RMSE for the testing sites is because there are 6,655 more fitting sites than the test sites.

As a special case for the bulk Pt(111) surface, the LED equation becomes

$$LED = NN^{Pt} \times e^{-a_1\varepsilon} \quad (14)$$

as there are no Ni atoms and $\overline{CN}^{Ni} = 0$. When there is no strain, ε is 0 and $e^{-a_1\varepsilon} = 1$. Thus, $LED = NN^{Pt} = 9$ due to the geometry of the Pt(111) crystal surface (six nearest neighbours in the surface layer and three nearest neighbours in the subsurface layer).

Data availability

All of the raw and processed experimental data are available via GitHub at https://github.com/AET-Nanocatalysts/Pt-Alloy.

Code availability

All of the MATLAB source codes for the 3D image reconstruction, atom tracing, refinement and data analysis in this work are available via GitHub at https://github.com/AET-Nanocatalysts/Pt-Alloy.

References

1. Friend, C. M. & Xu, B. Heterogeneous catalysis: a central science for a sustainable future. *Acc. Chem. Res.* **50**, 517–521 (2017).
2. Astruc, D. Introduction: nanoparticles in catalysis. *Chem. Rev.* **120**, 461–463 (2020).
3. Mitchell, S., Qin, R., Zheng, N. & Pérez-Ramírez, J. Nanoscale engineering of catalytic materials for sustainable technologies. *Nat. Nanotechnol.* **16**, 129–139 (2021).
4. Stamenkovic, V. R. et al. Improved oxygen reduction activity on $Pt_3Ni(111)$ via increased surface site availability. *Science* **315**, 493–497 (2007).
5. Nørskov, J. K. et al. The nature of the active site in heterogeneous metal catalysis. *Chem. Soc. Rev.* **37**, 2163–2171 (2008).
6. de Smit, E. et al. Nanoscale chemical imaging of a working catalyst by scanning transmission X-ray microscopy. *Nature* **456**, 222–225 (2008).
7. Greeley, J. et al. Alloys of platinum and early transition metals as oxygen reduction electrocatalysts. *Nat. Chem.* **1**, 552–556 (2009).
8. Strasser, P. et al. Lattice-strain control of the activity in dealloyed core–shell fuel cell catalysts. *Nat. Chem.* **2**, 454–460 (2010).
9. Lamberti, C., Zecchina, A., Groppo, E. & Bordiga, S. Probing the surfaces of heterogeneous catalysts by in situ IR spectroscopy. *Chem. Soc. Rev.* **39**, 4951–5001 (2010).
10. Chen, C. et al. Highly crystalline multimetallic nanoframes with three-dimensional electrocatalytic surfaces. *Science* **343**, 1339–1343 (2014).
11. Calle-Vallejo, F. et al. Finding optimal surface sites on heterogeneous catalysts by counting nearest neighbors. *Science* **350**, 185–189 (2015).
12. Zhang, L. et al. Platinum-based nanocages with subnanometer-thick walls and well-defined, controllable facets. *Science* **349**, 412–416 (2015).
13. Escudero-Escribano, M. et al. Tuning the activity of Pt alloy electrocatalysts by means of the lanthanide contraction. *Science* **352**, 73–76 (2016).
14. Kulkarni, A., Siahrostami, S., Patel, A. & Nørskov, J. K. Understanding catalytic activity trends in the oxygen reduction reaction. *Chem. Rev.* **118**, 2302–2312 (2018).
15. Núñez, M., Lansford, J. L. & Vlachos, D. G. Optimization of the facet structure of transition-metal catalysts applied to the oxygen reduction reaction. *Nat. Chem.* **11**, 449–456 (2019).
16. Wang, L. et al. Tunable intrinsic strain in two-dimensional transition metal electrocatalysts. *Science* **363**, 870–874 (2019).
17. Kim, S. et al. Correlating 3D surface atomic structure and catalytic activities of Pt nanocrystals. *Nano Lett.* **21**, 1175–1183 (2021).
18. Lee, J., Jeong, C., Lee, T., Ryu, S. & Yang, Y. Direct observation of three-dimensional atomic structure of twinned metallic nanoparticles and their catalytic properties. *Nano Lett.* **22**, 665–672 (2022).

19. Kluge, R. M. et al. A trade-off between ligand and strain effects optimizes the oxygen reduction activity of Pt alloys. *Energy Environ. Sci.* **15**, 5181–5191 (2022).
20. Li, M. et al. Ultrafine jagged platinum nanowires enable ultrahigh mass activity for the oxygen reduction reaction. *Science* **354**, 1414–1419 (2016).
21. Tao, F. et al. Reaction-driven restructuring of Rh–Pd and Pt–Pd core–shell nanoparticles. *Science* **322**, 932–934 (2008).
22. Cui, C., Gan, L., Heggen, M., Rudi, S. & Strasser, P. Compositional segregation in shaped Pt alloy nanoparticles and their structural behaviour during electrocatalysis. *Nat. Mater.* **12**, 765–771 (2013).
23. Zugic, B. et al. Dynamic restructuring drives catalytic activity on nanoporous gold–silver alloy catalysts. *Nat. Mater.* **16**, 558–564 (2017).
24. Jacobse, L., Huang, Y.-F., Koper, M. T. M. & Rost, M. J. Correlation of surface site formation to nanoisland growth in the electrochemical roughening of Pt(111). *Nat. Mater.* **17**, 277–282 (2018).
25. Timoshenko, J. & Roldan Cuenya, B. In situ/operando electrocatalyst characterization by X-ray absorption spectroscopy. *Chem. Rev.* **121**, 882–961 (2021).
26. Loukrakpam, R. et al. Nanoengineered PtCo and PtNi catalysts for oxygen reduction reaction: an assessment of the structural and electrocatalytic properties. *J. Phys. Chem. C* **115**, 1682–1694 (2011).
27. De Jonge, N. & Ross, F. M. Electron microscopy of specimens in liquid. *Nat. Nanotechnol.* **6**, 695–704 (2011).
28. Wu, J. et al. In situ environmental TEM in imaging gas and liquid phase chemical reactions for materials research. *Adv. Mater.* **28**, 9686–9712 (2016).
29. Tian, N., Zhou, Z.-Y., Sun, S.-G., Ding, Y. & Wang, Z. L. Synthesis of tetrahexahedral platinum nanocrystals with high-index facets and high electro-oxidation activity. *Science* **316**, 732–735 (2007).
30. Chattot, R. et al. Surface distortion as a unifying concept and descriptor in oxygen reduction reaction electrocatalysis. *Nat. Mater.* **17**, 827–833 (2018).
31. Tian, X. et al. Engineering bunched Pt–Ni alloy nanocages for efficient oxygen reduction in practical fuel cells. *Science* **366**, 850–856 (2019).
32. Miao, J., Ercius, P. & Billinge, S. J. Atomic electron tomography: 3D structures without crystals. *Science* **353**, aaf2157 (2016).
33. Scott, M. C. et al. Electron tomography at 2.4-ångström resolution. *Nature* **483**, 444–447 (2012).
34. Zhou, J. et al. Observing crystal nucleation in four dimensions using atomic electron tomography. *Nature* **570**, 500–503 (2019).
35. Yang, Y. et al. Determining the three-dimensional atomic structure of an amorphous solid. *Nature* **592**, 60–64 (2021).
36. Moniri, S. et al. Three-dimensional atomic structure and local chemical order of medium- and high-entropy nanoalloys. *Nature* **624**, 564–569 (2023).
37. Debe, M. K. Electrocatalyst approaches and challenges for automotive fuel cells. *Nature* **486**, 43–51 (2012).
38. Banham, D. & Ye, S. Current status and future development of catalyst materials and catalyst layers for proton exchange membrane fuel cells: an industrial perspective. *ACS Energy Lett.* **2**, 629–638 (2017).
39. Huang, X. et al. High-performance transition metal-doped Pt_3Ni octahedra for oxygen reduction reaction. *Science* **348**, 1230–1234 (2015).
40. Jia, Q. et al. Roles of Mo surface dopants in enhancing the ORR performance of octahedral PtNi nanoparticles. *Nano Lett.* **18**, 798–804 (2018).
41. Dionigi, F. et al. Controlling near-surface Ni composition in octahedral PtNi(Mo) nanoparticles by Mo doping for a highly active oxygen reduction reaction catalyst. *Nano Lett.* **19**, 6876–6885 (2019).
42. Polani, S. et al. Size and composition dependence of oxygen reduction reaction catalytic activities of Mo-doped PtNi/C octahedral nanocrystals. *ACS Catal.* **11**, 11407–11415 (2021).
43. Tran, K. & Ulissi, Z. W. Active learning across intermetallics to guide discovery of electrocatalysts for CO_2 reduction and H_2 evolution. *Nat. Catal.* **1**, 696–703 (2018).
44. Zhong, M. et al. Accelerated discovery of CO_2 electrocatalysts using active machine learning. *Nature* **581**, 178–183 (2020).
45. Nørskov, J. K. et al. Origin of the overpotential for oxygen reduction at a fuel-cell cathode. *J. Phys. Chem. B* **108**, 17886–17892 (2004).
46. Nanba, Y. & Koyama, M. An element-based generalized coordination number for predicting the oxygen binding energy on Pt_3M (M=Co, Ni, or Cu) alloy nanoparticles. *ACS Omega* **6**, 3218–3226 (2021).
47. Calle-Vallejo, F. & Bandarenka, A. S. Enabling generalized coordination numbers to describe strain effects. *ChemSusChem* **11**, 1824–1828 (2018).
48. Wang, C. et al. Correlation between surface chemistry and electrocatalytic properties of monodisperse Pt_xNi_{1-x} nanoparticles. *Adv. Funct. Mater.* **21**, 147–152 (2011).
49. Lee, J. D. et al. Tuning the electrocatalytic oxygen reduction reaction activity of Pt–Co nanocrystals by cobalt concentration with atomic-scale understanding. *ACS Appl. Mater. Interfaces* **11**, 26789–26797 (2019).
50. Shinozaki, K., Zack, J. W., Richards, R. M., Pivovar, B. S. & Kocha, S. S. Oxygen reduction reaction measurements on platinum electrocatalysts utilizing rotating disk electrode technique. *J. Electrochem. Soc.* **162**, F1144–F1158 (2015).
51. Dabov, K., Foi, A., Katkovnik, V. & Egiazarian, K. Image denoising by sparse 3-D transform-domain collaborative filtering. *IEEE Trans. Image Process.* **16**, 2080–2095 (2007).
52. Yang, Y. et al. Deciphering chemical order/disorder and material properties at the single-atom level. *Nature* **542**, 75–79 (2017).
53. Chen, C.-C. et al. Three-dimensional imaging of dislocations in a nanoparticle at atomic resolution. *Nature* **496**, 74–77 (2013).
54. Otsu, N. A threshold selection method from gray-level histograms. *IEEE Trans. Syst. Man. Cybern.* **9**, 62–66 (1979).
55. Pham, M., Yuan, Y., Rana, A., Osher, S. & Miao, J. Accurate real space iterative reconstruction (RESIRE) algorithm for tomography. *Sci. Rep.* **13**, 5624 (2023).
56. Jia, Q. et al. Activity descriptor identification for oxygen reduction on platinum-based bimetallic nanoparticles: in situ observation of the linear composition–strain–activity relationship. *ACS Nano* **9**, 387–400 (2015).
57. Newville, M. IFEFFIT: interactive XAFS analysis and FEFF fitting. *J. Synchrotron Radiat.* **8**, 322–324 (2001).
58. Ravel, B. & Gallagher, K. Atomic structure and the magnetic properties of Zr-doped Sm_2Co_{17}. *Phys. Scr.* **2005**, 606 (2005).
59. Newville, M., Līviņš, P., Yacoby, Y., Rehr, J. J. & Stern, E. A. Near-edge x-ray-absorption fine structure of Pb: a comparison of theory and experiment. *Phys. Rev. B* **47**, 14126–14131 (1993).
60. Ankudinov, A. L., Ravel, B., Rehr, J. J. & Conradson, S. D. Real-space multiple-scattering calculation and interpretation of x-ray-absorption near-edge structure. *Phys. Rev. B* **58**, 7565–7576 (1998).
61. Do Carmo, M. P. *Differential Geometry of Curves and Surfaces* 2nd edn (Dover Publications, 2016).
62. Lechner, W. & Dellago, C. Accurate determination of crystal structures based on averaged local bond order parameters. *J. Chem. Phys.* **129**, 114707 (2008).
63. Li, Q.-J., Sheng, H. & Ma, E. Strengthening in multi-principal element alloys with local-chemical-order roughened dislocation pathways. *Nat. Commun.* **10**, 3563 (2019).

64. Mortensen, J. J. et al. GPAW: an open Python package for electronic structure calculations. *J. Chem. Phys.* **160**, 092503 (2024).
65. Larsen, A. H. et al. *J. Condens. Matter Phys.* **29**, 273002 (2017).
66. Kresse, G. & Hafner, J. Ab initio molecular dynamics for liquid metals. *Phys. Rev. B* **47**, 558–561 (1993).
67. Kresse, G. & Hafner, J. Ab initio molecular-dynamics simulation of the liquid-metal–amorphous-semiconductor transition in germanium. *Phys. Rev. B* **49**, 14251–14269 (1994).
68. Kresse, G. & Furthmüller, J. Efficient iterative schemes for ab initio total-energy calculations using a plane-wave basis set. *Phys. Rev. B* **54**, 11169–11186 (1996).
69. Kresse, G. & Furthmüller, J. Efficiency of ab-initio total energy calculations for metals and semiconductors using a plane-wave basis set. *Comput. Mater. Sci.* **6**, 15–50 (1996).
70. Mortensen, J. J., Hansen, L. B. & Jacobsen, K. W. Real-space grid implementation of the projector augmented wave method. *Phys. Rev. B* **71**, 035109 (2005).
71. Enkovaara, J. et al. Electronic structure calculations with GPAW: a real-space implementation of the projector augmented-wave method. *J. Phys. Condens. Matter* **22**, 253202 (2010).
72. Kresse, G. & Joubert, D. From ultrasoft pseudopotentials to the projector augmented-wave method. *Phys. Rev. B* **59**, 1758–1775 (1999).
73. Perdew, J. P., Burke, K. & Ernzerhof, M. Generalized gradient approximation made simple. *Phys. Rev. Lett.* **77**, 3865–3868 (1996).
74. Rasmussen, C. E. in *Advanced Lectures on Machine Learning* (eds Bousquet, O. et al.) 63–71 (Springer, 2003).
75. Himanen, L. et al. DScribe: library of descriptors for machine learning in materials science. *Comput. Phys. Commun.* **247**, 106949 (2020).
76. Bartók, A. P., Kondor, R. & Csányi, G. On representing chemical environments. *Phys. Rev. B* **87**, 184115 (2013).
77. Pedregosa, F. et al. Scikit-learn: machine learning in Python. *J. Mach. Learn. Res.* **12**, 2825–2830 (2011).
78. Viswanathan, V., Hansen, H. A., Rossmeisl, J. & Nørskov, J. K. Universality in oxygen reduction electrocatalysis on metal surfaces. *ACS Catal.* **2**, 1654–1660 (2012).

Acknowledgements

This work was primarily supported by the US Department of Energy (DOE), Office of Science, Basic Energy Sciences (BES), Division of Materials Sciences and Engineering under award DE-SC0010378 (including the AET experiments, 3D image reconstruction, atom tracing, classification and data analysis). It was also partially supported by the NSF DMREF under award number DMR-1437263. G.S. and P.S. acknowledge support by DOE-BES grant DE-SC0019152. AET experiments were performed with TEAM I at the Molecular Foundry, which is supported by the Office of Science, Office of Basic Energy Sciences of the US DOE under contract number DE-AC02-05CH11231. The XAS experiments were conducted on beamline 8-ID (ISS) of the National Synchrotron Light Source II, which is supported by the Office of Science, Office of Basic Energy Sciences of the US DOE under contract number DE-SC0012704.

Author contributions

J.M. directed the project; Z.Z., Y.L. and Y.H. synthesized the samples and performed the ORR test; J.Z., P.E., J.C. and J.M. discussed and/or conducted the AET experiments; Q.J. and Q.S. did the XAS experiments; Yao Yang, Yongsoo Yang, Y. Yuan and J.M. performed the 3D image reconstruction, atom tracing and classification; G.S., Z.W. and P.S. carried out the DFT calculations and implemented the ML method with input from Yao Yang, C.O. and J.M.; Yao Yang, J.Z., Z.Z., G.S., C.O., S.M., C.Z., H.H., P.S., Y.H. and J.M. analysed and/or interpreted the results. J.M., Yao Yang, S.M., Z.Z. and G.S. wrote the manuscript. All authors commented on the manuscript.

Competing interests

The authors declare no competing interests.

Additional information

Supplementary information The online version contains supplementary material available at https://doi.org/10.1038/s41929-024-01175-8.

Correspondence and requests for materials should be addressed to Philippe Sautet, Yu Huang or Jianwei Miao.

Peer review information *Nature Catalysis* thanks Jasna Jankovic, Michihisa Koyama and Woong Hee Lee for their contribution to the peer review of this work.